Effects of surface tension on the Richtmyer-Meshkov instability in fully compressible and inviscid fluids

Kaitao Tang,[1,2] Wouter Mostert,[1,3] Daniel Fuster,[4] and Luc Deike[1,5]
[1]*Department of Mechanical and Aerospace Engineering, Princeton University, Princeton, New Jersey 08544, USA*
[2]*Center for Combustion Energy and School of Aerospace Engineering, Tsinghua University, Beijing 100084, China*
[3]*Department of Mechanical and Aerospace Engineering, Missouri University of Science and Technology, Rolla, Missouri 65401, USA*
[4]*Sorbonne Université, Centre National de la Recherche Scientifique, UMR 7190, Institut Jean Le Rond D'Alembert, F-75005 Paris, France*
[5]*High Meadows Environmental Institute, Princeton University, Princeton, New Jersey 08544, USA*

(Received 5 March 2021; accepted 25 October 2021; published 17 November 2021)

Novel numerical simulations investigating the Richtmyer-Meshkov instability (RMI) with surface tension are presented. We solve the two-phase compressible Euler equation with surface tension and interface reconstruction by a volume-of-fluid method. We validate and bridge existing theoretical models of effects of surface tension on the RMI in the linear, transitional, and nonlinear postshock growth regimes. After deriving a consistent nondimensional formulation from an existing linear incompressible theory predicting perturbation development under large surface tension, we find good agreement with theoretical prediction in the small-amplitude (linear) oscillatory regime for positive Atwood numbers, and we show that negative Atwood numbers can be accommodated by an appropriate modification to the theory. Next, we show good agreement with nonlinear theory for asymptotic interface growth in the limit of small surface tension. Finally, we use the nondimensional formulation to define a heuristic criterion which identifies the transition from the linear regime to the nonlinear regime at intermediate surface tension. These results highlight the utility of this numerical method for compressible problems featuring surface tension, and they pave the way for a broader investigation into mixed compressible/incompressible problems.

DOI: 10.1103/PhysRevFluids.6.113901

I. INTRODUCTION

The Richtmyer-Meshkov instability (RMI) occurs when two regions of fluids with different densities and separated by a perturbed interface are subjected to the passage of a shock wave, which is oftened modeled as an impulsive acceleration. The misalignment of the pressure and density gradients incurred by the shock-interface interaction results in the baroclinic generation of vorticity deposited on the interface, and hence in the subsequent growth and development of perturbations. The RMI is relevant to many applications: it is well-known to inhibit the attainment of fusion in inertial confinement fusion contexts [1]; it can enhance mixing in high-speed airbreathing engines [2]; and may also drive mixing in certain supernovae [3] and magnetic field amplification in supernova remnants traveling through the interstellar medium [4].

If at least one of the fluids is a liquid, or if the interface between the fluids is a membrane [5], then surface tension may play a role. This is the case for the familiar example of dropping a bucket

filled with water on the ground [6]; the impact on the ground constitutes an impulsive acceleration which promotes the RMI on the water surface. Compressible effects in the gas phase are explicitly involved in the problem of high-speed droplet aerobreakup, which is challenging to investigate both in the laboratory (see Theofanous [7] and references therein) and numerically [8]. In this connection, the RMI may be relevant to the early-time behavior of the shocked droplet. In any case, the effect of surface tension on the fine-scale structures at these early times is typically not accounted for and clarified by large-scale numerical simulations on grounds of insufficient resolution, even with adaptive mesh refinement (AMR) techniques (e.g., as noted by Meng and Colonius [8]).

As a fundamental problem, the effects of surface tension on the RMI, along with the closely-related Rayleigh-Taylor instability (RTI), have seen prior investigation. Mikaelian [5] performed a linear stability analysis, finding that the (sufficiently strong) surface tension induces a stable oscillation in the shocked interface whose amplitude and frequency depend on the magnitude of the surface tension. Bigdelou [9] recently conducted a series of numerical simulations on shock-driven multiphase flow problems using the level-set method [10], where Mikaelian's predictions [5] are used for a brief validation of the numerical model (see their Fig. 4.49). If the surface tension is sufficiently weak, then the interface enters a nonlinear growth regime featuring asymmetrically formed narrow "spike" and broad "bubble" structures interpenetrating between the fluids [11,12]; in this regime, Sohn [13] provided an asymptotic analysis of the velocity of the bubble-structures and included a brief numerical verification using a phase-field interface model [14] in incompressible fluids. Matsuoka [15] also studied the interfacial behavior in incompressible RMI with surface tension by numerically solving the Birkhoff-Rott equation for vortex sheet motion, and demonstrated that large surface tension is able to stabilize the interface and suppress its late-time rollup behavior. The weakly nonlinear RTI under the effect of surface tension has also been investigated in a variety of studies; see, e.g., Garnier *et al.* [16] and Guo *et al.* [17]. For a broad review of studies of the RTI and RMI including surface tension are covered, among other topics, see the review of Zhou [18].

The existing studies reveal only a limited understanding of the RMI with surface tension. First, the stabilizing effect of surface tension on the RMI suggests that it may inhibit transition to the nonlinear regime of bubble and spike development. However, for sufficiently large Weber numbers (defined as the ratio between inertial and surface tension forces), the interface perturbations may grow large enough to escape the linear regime before reaching the maximum amplitude of oscillation, so that Mikaelian's analysis [5] no longer applies. This introduces a *critical Weber number* for the RMI with surface tension, which to our knowledge has not been systematically studied besides a brief heuristic calculation by Bigdelou [9], whose numerical validation is conducted in the linear regime. Second, this critical value will not in general correspond with the vanishingly small surface tension required by Sohn's [13] asymptotic analysis; we expect that there exist cases with intermediately small surface tensions (that is, large Weber numbers) whose perturbation growth patterns are currently not well understood. Finally, besides Bigdelou [9], none of these studies, which rely on numerical support of theoretical results, consider the effects of compressible flow, which may appear, for example, in the case of shocked-membrane problems arising in shock tube environments [5], or in shock-bubble interactions [19] where to our knowledge the very early time-evolution of the shocked bubble under the influence of surface tension has not been investigated in detail. This may be partly due to the relative lack of compressible-flow solvers that include surface tension effects, although there has been recent progress in this direction (see, e.g., Ref. [20], used as the basis for this study, and Refs. [9,21]).

In this study we present fully nonlinear, compressible numerical simulations of the inviscid RMI with surface tension, using Fuster and Popinet's [20] recently developed and implemented numerical technique in the Basilisk package. In addition to the technical significance of this study, its purpose is, first, to provide numerical support for the studies of Mikaelian [5] and Sohn [13] in a compressible environment; second, to provide insight into the nonlinear development of the problem, considering especially the asymptotic large-time behavior at small surface tensions (large Weber numbers); and finally, to find the critical Weber number required to suppress the RMI and, in particular, to restrict oscillations of the perturbation to the linear regime.

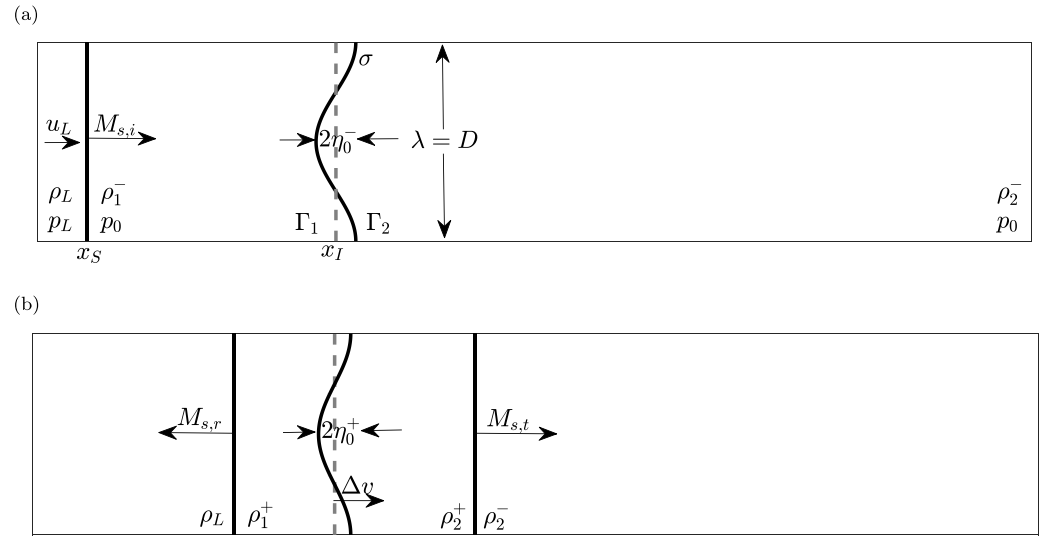

FIG. 1. Sketches for the pre- (a) and postshock (b) states of the compressible RMI problem with surface tension. The domain is separated by a sinusoidal interface featuring initial amplitude η_0^- and wavelength λ. The fluids to the left and right of the interface are labeled "1" and "2," respectively. The incident shock with Mach number $M_{s,I}$ changes the state of fluid 1 from preshock (with superscript "$-$") to intermediate (with subscript "L") before its interaction with the interface, which compresses the interfacial perturbation to η_0^+. The transmitted shock and reflected wave bring the two fluids to their final postshock states (with superscript "+"), while the interface perturbation develops under the influence of surface tension σ.

Our study is structured as follows. In Sec. II we adapt the theoretical work of Mikaelian [5] on the RMI perturbation development under large surface tension [with typical postshock Weber number $\mathrm{We}^+ < 10^2$, as defined in Eq. (7)] to form a fully nondimensional framework, based on which the following analyses are conducted. In Sec. III we present a formulation of the problem and introduce the numerical method. Afterwards, with the postshock parameters determined, we compare Mikaelian's [5] theory with the scaled numerical results in Sec. IV A, and propose a modified theoretical model based on Vandenboomgaerde *et al.* [22] to better account for both positive and negative Atwood numbers. For the development of nonlinear perturbation structures in the limit of small surface tension ($\mathrm{We}^+ > 10^3$), we discuss the theory of Sohn [13] and compare it with the scaled numerical results in Sec. IV B, although a complete comparison of the relative large-time nonlinear behavior of bubbles and spikes at varying Weber numbers remains a topic for future study. Then in Sec. IV C we use the nondimensional framework to identify the transitional nonlinear development of the interface at intermediate surface tension ($10^2 < \mathrm{We}^+ < 10^3$), and hence to propose a heuristic criterion to delineate the transition to nonlinear development. We conclude the study in Sec. V with some remarks on future work.

II. NONDIMENSIONAL SCALING MODEL

We first adapt the theoretical result from a linear stability analysis of the incompressible RMI with surface tension, due to Mikaelian [5], into a nondimensional formulation which can then be interpreted in the compressible flow problem featuring a shock wave.

The flow configuration is illustrated in Fig. 1, where the fluid to the left is labeled "1," and the fluid to the right labeled "2." Initially, the velocities of the two inviscid fluids and the sinusoidally perturbed interface are all set to zero. The incident shock travels rightwards from the left boundary $x = x_S$ to hit the interface, whose passage will first bring the density and pressure in fluid 1 to

intermediate values denoted by subscript "L." As is shown in Fig. 1(b), after the shock-interface interaction, the interface will be accelerated and acquire a velocity jump Δv; in the meanwhile, part of the shock energy will be transferred into fluid 2 in the form of a transmitted shock, and the rest will reflect back into fluid 1 as a reflected wave, whose passage will bring the density and pressure in fluid 1 to their postshock values. The perturbed interface will then evolve under the influence of surface tension σ.

The nondimensional groups governing the problem can be derived with respect to pre- and postshock state of the interface. We first discuss the preshock state, which represents the *a priori* understanding of the system, before next discussing the postshock state, to which Mikaelian's analysis [5] naturally applies. Afterwards, we will discuss how the postshock state may be determined from knowledge of the preshock state. In the following, minus-sign superscripts denote the preshock state, and plus-sign superscripts denote postshock state.

A. Preshock dimensionless parameters

We discuss the state of the problem prior to the shock-interface interaction. The densities of the preshock fluids are ρ_i^- $(i = 1, 2)$, the unperturbed pressure in each fluid is p_0 and the specific heat ratio of each fluid is Γ_i. The fluids are considered inviscid in this model. The interface which separates the fluids has a monochromatic, sinusoidal perturbation of wavelength λ and amplitude η_0^-, and corresponding wave number $k = 2\pi/\lambda$.

The surface tension is given by σ. The corrugated interface slightly perturbs the pressure in the two fluid by the action of surface tension; which may be approximated as $\Delta p = 2\sigma/R_c = 2\sigma\eta_0^- k^2$, where we use the Young-Laplace equation and take the characteristic radius of curvature R_c as that at the extrema of the sinusoidal interface. In our work, the maximum magnitude of the ratio $\Delta p/p_0$ is 10^{-2}; thus, we conclude that this pressure-perturbation Δp has negligible effect on the subsequent evolution of the system.

The incident shock is planar with a speed $u_{s,I}$ and induces a velocity u_L in fluid 1, which is known analytically from the Rankine-Hugoniot shock relations. Applying Buckingham's theorem, we form the following four dimensionless groups apart from Γ_i:

$$s^- \equiv \eta_0^- k = 2\pi \frac{\eta_0^-}{\lambda}, \quad A^- \equiv \frac{\rho_2^- - \rho_1^-}{\rho_2^- + \rho_1^-}, \quad \mathrm{We}^- \equiv \frac{\rho_1^- + \rho_2^-}{\sigma k} A^{-2} u_L^2, \quad M_{s,I} = \frac{u_{s,I}}{\sqrt{\Gamma_1 p_0/\rho_1^-}}, \tag{1}$$

where s^- characterizes the slope of the initial perturbed interface; A^- is the Atwood number, which represents the initial density setup; We^- is the Weber number, which measures the strength of surface tension, and $M_{s,I}$ is the Mach number of incident shock, which satisfies $M_{s,I} > 1$. It should be noted that the following incident shock strength $\epsilon \in (0, 1)$, defined as the relative pressure change in Fluid 1 after the passage of the incident shock, is sometimes used instead of $M_{s,I}$ within literature (e.g., Refs. [22,23]) and may be calculated from $M_{s,I}$ and Γ_1 using the Rankine-Hugoniot shock relation,

$$\epsilon \equiv 1 - \frac{p_0}{p_L} = \frac{2\Gamma_1\left(M_{s,I}^2 - 1\right)}{\Gamma_1\left(2M_{s,I}^2 - 1\right) + 1}. \tag{2}$$

B. Postshock dimensionless parameters

We will now discuss the application of Mikaelian's incompressible, impulsive model [5] to the compressible case, and develop the appropriate dimensionless parameters. Mikaelian predicts that, if the perturbation development is in the linear regime (i.e., when the slope s remains small), and the effect of compressibility is negligible after the shock-interface interaction, surface tension will act

as a restoring force and cause the postshock perturbation amplitude $\eta(t)$ to oscillate sinusoidally,

$$\eta(t) = \eta_0^+ \cos(\omega t) + \frac{\dot{\eta}_0^+}{\omega} \sin(\omega t) = \eta_0^+ \sqrt{1 + \left(\frac{\dot{\eta}_0^+}{\eta_0^+ \omega}\right)^2} \sin\left(\omega t + \arctan \frac{\eta_0^+ \omega}{\dot{\eta}_0^+}\right), \tag{3}$$

where η_0^+ is the postshock initial perturbation amplitude, and the capillary angular frequency ω is defined in the following form, with postshock fluid densities ρ_1^+ and ρ_2^+:

$$\omega = \sqrt{\frac{k^3 \sigma}{\rho_1^+ + \rho_2^+}}. \tag{4}$$

$\dot{\eta}_0^+$ is the postshock initial perturbation growth rate, which Mikaelian [5] gives as

$$\dot{\eta}_0^+ = \Delta v k A^+ \eta_0^+, \tag{5}$$

where the postshock Atwood number $A^+ \equiv (\rho_2^+ - \rho_1^+)/(\rho_2^+ + \rho_1^+)$, and Δv is the postshock velocity jump of the interface. Equation (5) is identical to Richtmyer's [24] prescription for growth rate in the RMI without surface tension. Equations (4) and (5) combined yield the following result:

$$\left(\frac{\dot{\eta}_0^+}{\eta_0^+ \omega}\right)^2 = \frac{(\rho_1^+ + \rho_2^+) A^{+2} \Delta v^2}{\sigma k}. \tag{6}$$

The term $(\dot{\eta}_0^+/\eta_0^+ \omega)^2 = \mathrm{We}^+$ is a postshock Weber number of the perturbed interface and measures the relative importance of the inertia of the flow compared to the surface tension. A set of dimensionless groups to describe the growth characteristics of the RMI can be further defined in terms of postshock variables to be

$$s^+ = 2\pi \frac{\eta_0^+}{\lambda}, \quad A^+ \equiv \frac{\rho_2^+ - \rho_1^+}{\rho_2^+ + \rho_1^+}, \quad \mathrm{We}^+ \equiv \left(\frac{\dot{\eta}_0^+}{\eta_0^+ \omega}\right)^2 = \frac{\rho_1^+ + \rho_2^+}{\sigma k} A^{+2} \Delta v^2. \tag{7}$$

These are of the same form as the preshock parameters, and both will be used throughout this work. According to Eq. (3), the time-dependent amplitude $\eta(t) \equiv \eta$ depends on $\sqrt{1 + \mathrm{We}^+}$. Further, combining Eqs. (4) with (7) yields $\omega = A^+ \Delta v k / \sqrt{\mathrm{We}^+}$. These can be used to nondimensionalize amplitude and time t by

$$\tilde{\eta} \equiv \frac{\eta}{\eta_0^+ \sqrt{1 + \mathrm{We}^+}}, \quad \tilde{t} \equiv \omega t = \frac{k A^+ \Delta v}{\sqrt{\mathrm{We}^+}} t, \tag{8}$$

where the tildes indicate nondimensional variables. With these parameters introduced, Mikaelian's model Eq. (3) can be summarized in the following normalized form:

$$\tilde{\eta} = \sin\left(\tilde{t} + \arctan \frac{1}{\sqrt{\mathrm{We}^+}}\right). \tag{9}$$

We note that saturation at $\tilde{t} = \pi/2 - \arctan(1/\sqrt{\mathrm{We}^+})$, in the regime discussed by Mikaelian [5] and in which our Eq. (9) is presented, is governed by linear processes dependent on strong surface tension. However, for small surface tensions nonlinear effects in underlying instability come to dominate, which cannot be predicted by Eq. (9); but the postshock normalization scheme Eq. (8) may still be used for comparison with strong surface tension cases, especially for the transition to nonlinear regime with intermediate surface tension, as will be discussed in Sec. IV C.

It is of interest to understand the relation between preshock and postshock parameters. It has been concluded in Velikovich [25] that in the weak-shock limit (incident shock strength $\epsilon \to 0$), the pre- and postshock values of perturbation slope, Weber and Atwood number are close and there is no need to distinguish between them. It is also in the same weak-shock limit that Richtmyer's prescription is reported to give most accurate results (see, for example, Fig. 1 in Velikovich *et al.*

[26].) In general, however, the postshock parameters may deviate significantly from the preshock values. For the present study, the postshock parameters are determined numerically. For a discussion on its effectiveness in comparison with alternative methods, see Appendix B.

Finally, a change in sign of the preshock Atwood number A^- may introduce a qualitative change in the shock interaction process [22,27,28]. When the shock wave interacts with the interface, it undergoes a refraction process which results in a transmitted shock and a reflected wave, which may be a shock or a rarefaction wave. The reflected wave type depends on A^- and Γ_i. Drake [27] identifies the following critical preshock Atwood number A_c^- for an unperturbed interface,

$$A_c^- = \frac{\Gamma_1 - \Gamma_2}{\Gamma_1 + \Gamma_2 + 2}. \tag{10}$$

When $A^- < A_c^-$, a reflected rarefaction is expected to form in fluid 1; otherwise, a reflected shock is expected. Within our work, we set the specific heat ratios as $\Gamma_1 = \Gamma_2 = 1.4$; hence, $A_c^- = 0$, i.e., negative preshock Atwood numbers A^- correspond to reflected rarefactions and positive ones to reflected shocks. This effect is not accounted for in Mikaelian's model [5]; its consequences will be examined in Sec. IV A.

III. FORMULATION AND METHODOLOGY

A. Governing equations

We solve the two-phase compressible Euler equations with surface tension, which are written in their averaged dimensional form,

$$\frac{\partial \rho}{\partial t} + \nabla \cdot (\rho \boldsymbol{u}) = 0, \tag{11}$$

$$\frac{\partial \rho \boldsymbol{u}}{\partial t} + \nabla \cdot (\rho \boldsymbol{u}\boldsymbol{u}) = -\nabla p + \sigma \kappa \delta_s \boldsymbol{n}, \tag{12}$$

$$\frac{\partial}{\partial t}\left(\rho e + \frac{1}{2}\rho \boldsymbol{u}^2\right) + \nabla \cdot \left[\boldsymbol{u}\left(\rho e + \frac{1}{2}\rho \boldsymbol{u}^2\right)\right] = -\nabla \cdot (\boldsymbol{u} p) + \sigma \kappa \delta_s \boldsymbol{n} \cdot \boldsymbol{u}. \tag{13}$$

Equations (11) and (12) are, respectively, the continuity and momentum equation, where p is the fluid pressure. The influence of surface tension is incorporated as the volumetric term $\sigma \kappa \delta_s \boldsymbol{n}$ within Eq. (12), where σ is the surface-tension coefficient, κ and $\boldsymbol{n}$ the local curvature and normal vector on the interface. The Dirac δ_s is nonzero only on the interface, indicating the local concentration of surface tension effects [29,30]. The energy Eq. (13) is included owing to the presence of compressibility, where e denotes the specific internal energy. Following Ref. [20], influences of thermal diffusion and mass transfer are neglected. Equations of state are still required to close the equation system. While both incompressible and compressible fluids can be modeled simultaneously by Mie-Grüneisen equation of state in the numerical solver, for this study we restrict our attention to entirely compressible flow by applying the ideal gas law as a special case:

$$\rho_i e_i = \frac{p_i}{\Gamma_i - 1}, \tag{14}$$

where $\rho_i,\ e_i,\ p_i\ (i = 1, 2)$ are, respectively, the density, specific internal energy and pressure of each fluid.

The following advective Eq. (15) is applied to determine the interface position, featuring a tracer function f that distinguishes between fluids 1 and 2 [20]:

$$\frac{\partial f}{\partial t} + \boldsymbol{u} \cdot \nabla f = 0. \tag{15}$$

Finally, in Fig. 1, the wavelength λ, wave number k, and postshock perturbation growth rate $\dot{\eta}_0^+$ suffice to provide natural reference scales for the length, mass and time quantities that appear in the

system Eqs. (15)–(13). Thus, following the work of Dimonte [31,32], the nondimensional variables,

$$\frac{\eta}{\lambda}, \quad \frac{u}{|\dot{\eta}_0^+|}, \quad k|\dot{\eta}_0^+|t, \tag{16}$$

will be used in the remainder of the study as an alternative to the nondimensional parameters presented in Sec. II.

B. Numerical method

The simulations in this work are conducted within the open-source solver Basilisk using the all-Mach scheme proposed by Fuster and Popinet [20] for multiphase flows, which is capable of handling mixed compressible-incompressible fluids. This is a second-order accurate finite volume numerical scheme with hyperbolic upwinding suitable for shock capturing. Within the solver, the mass and energy conservation Eqs. (11) and (13) are solved separately for each phase, while the geometric volume-of-fluid (VOF) reconstruction method guarantees a sharp representation of the fluid interface and reduces the parasitic currents induced by surface tension. For modeling of surface tension effects, $\delta_s \boldsymbol{n}$ in Eq. (12) is approximated as the gradient of the VOF tracer $\boldsymbol{\nabla} f$ following Brackbill's method [33], and the curvature κ is calculated by taking the finite-difference approximation of the derivatives of interface height functions [29].

The problem is initialized within a rectangular simulation domain of size $nD \times D$, where D is the width of the domain and $n = 5$, 7, or 11, depending on the particular case. The shock is initialized at the left boundary, so that the domain is defined by $\Omega = [x_S, nD + x_S] \times [-D, 0]$. The boundary conditions on the top and bottom of the domain are periodic. We use a zero-gradient boundary condition at the right boundary, while at the left side Dirichlet conditions are applied according to the postshock conditions for a incident shock of Mach number M_s; these are discussed further below.

The fluid interface is initially a cosine function of the form $x(y)/\lambda = x_I/\lambda + (\eta_0^-/\lambda)\cos ky$ where λ is set to the domain size D. The average position of the interface x_I/λ is set to 0. The incident shock is initialized at the left boundary of the simulation domain, at $x = x_S$ by assigning the values of ρ_L, q_L, E_L to the conservative variables via the aforementioned Dirichlet boundary conditions. We set the left boundary x_S immediately next to the initial interface at $x_I = 0$, so that the surface-tension-induced self-oscillation behavior does not have sufficient time to influence the preshock perturbation amplitude before its interaction with the incident shock.

The discretized grid size, being the same in x and y direction, is defined as $h = D/2^L$, where L is the resolution level. Most of our simulations are conducted on $L = 9$, while for convergence studies we also run certain cases on levels $L = 8$ and $L = 10$ for comparison. The discretized timestep is characterized and controlled by a nondimensional constant $CFL_{ac} = (c_m + u_m)\Delta t/h$, where c_m and u_m are the magnitudes of the expected maximum local speed of sound and the fluid velocity, respectively. For simulations conducted in this work, we set $CFL_{ac} = 0.5$ and 0.25 for strong-shock and weak-shock cases, respectively.

We now present the preshock nondimensional parameter space to be investigated in this work. Namely, we conduct the simulations with preshock slope s^- values going from low (0.02π), medium (0.03π) to high (0.04π), all of which are sufficiently small to satisfy the linear regime prerequisite $s^- \ll 1$. We thus allocate approximately 5–10 grid cells across the initial perturbation profile at resolution level $L = 9$, which is sufficient to capture the growth characteristics of the RMI independent of the numerical resolution, as shown in Sec. III A. We set $M_{s,I} = 2$ (strong-shock, corresponding to incident shock strength $\epsilon = 0.78$) in most situations, where influence of compressibility is already nontrivial but has not yet caused significant deviations from the impulsive model (see Fig. 8 in Ref. [34]), while also setting $M_{s,I} = 1.2$ (weak-shock, corresponding to $\epsilon = 0.40$) in certain cases to allow for discussions on its influence. Preshock Atwood numbers are set as $A^- = 9/11$ and $-9/11$. The magnitude of preshock Weber numbers We^- we investigate ranges from 10^1 to 10^3, which covers all three of the linear, transitional and nonlinear postshock growth-rate regime.

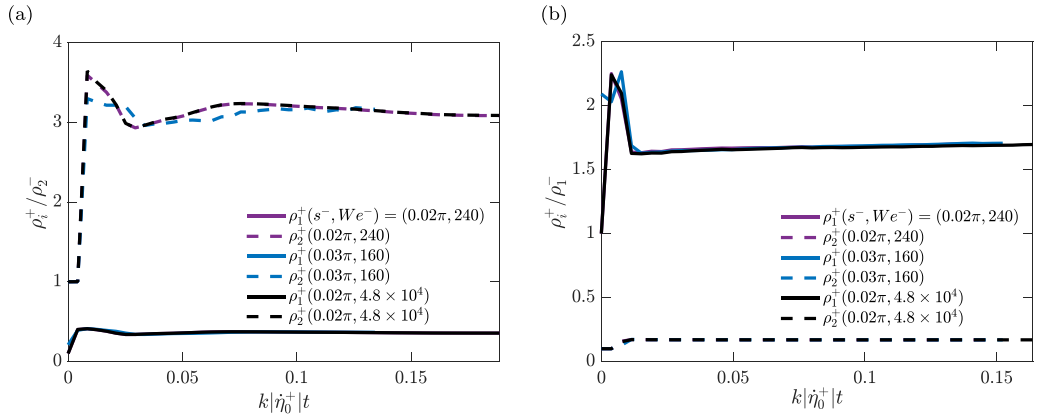

FIG. 2. The development of postshock density values ρ_i^+ in cases with preshock Atwood number $A^- = 9/11$ (a) and $A^- = -9/11$ (b) measured from numerical diagnostics. The postshock densities of the two fluids are observed to eventually settle down at steady-state values, which are chosen as the postshock values determined by numerical diagnostics.

IV. RESULTS

A. Linear regime

Mikaelian's existing theory is written in terms of the postshock state, which is not known *a priori* in this study. We therefore determine the postshock state, characterized by ρ_1^+, ρ_2^+, Δv, and η^+ numerically. This sets postshock dimensionless parameters s^+, A^+ and We^+, as discussed in Sec. IV B, where we find the postshock Atwood numbers A^+ to be 0.793 and -0.819, corresponding to the light-heavy and heavy-light density configurations.

In the diagnostics, the postshock state variables are extracted close to the interface, and averaged over y to remove variations due to the interface perturbation. Then we nondimensionalize the postshock variables by the natural units introduced in Sec. III A. Figure 2 shows the numerical outputs for sample cases with $A^- = \pm 9/11$, $\mathrm{We}^- = 160, 240$, and $s^- = 0.02\pi, 0.03\pi$.

All measured variables behave similarly in the diagnostics: there is a short transient period at early times associated with shock-interface interaction, before the measured variables stabilize as the transmitted and reflected wavefronts move away from the postshock interface. The steady-state values are not affected by the value of s^-, as expected, and are taken as the postshock state. As discussed in the Appendix B, these numerical diagnostics are more reliable for the present study than theoretical alternatives. Note that the density remaining constant after the initial transients supports the assumption that compressible effects are limited to the time during and immediately after the shock-interface interaction, and that the flow is approximately incompressible afterwards. This is consistent with conclusions from other numerical studies [6,35].

We now test the normalized model of Mikaelian [5] given by Eq. (9), which predicts a relationship between the nondimensional amplitude $\tilde{\eta}$ and the nondimensional time $\tilde{t}$ independent of the other nondimensional parameters (provided that the postshock Weber numbers We^+ are larger than 200, which causes an error less than 4.5% at the first peak if the phase shift term $\arctan 1/\sqrt{\mathrm{We}^+}$ is neglected).

The results are presented in Fig. 3, where they are organised into three major categories: strong shock ($M_{s,I} = 2$) with positive Atwood number ($A^- = 9/11$) in the first row, strong shock with negative Atwood number ($A^- = -9/11$) in the second and weak shock ($M_{s,I} = 1.2$) with positive Atwood number in the third row. For each Atwood/Mach number category, a sweeping of Weber number We^- is conducted. In the left column [Figs. 3(a), 3(c) and 3(e)], the amplitude and time are normalized naturally (see Sec. III); in the right column, the scaled amplitude and time based

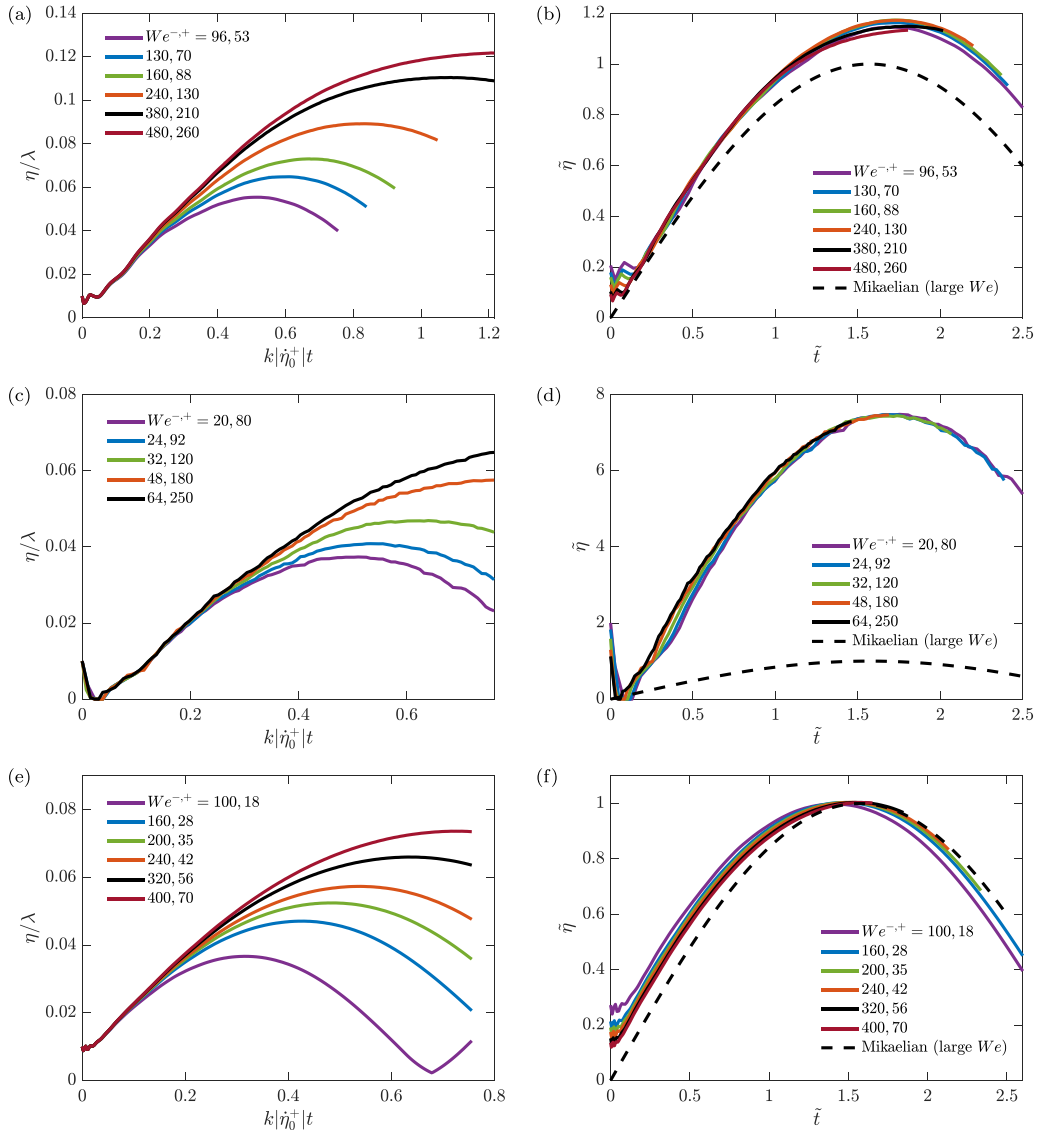

FIG. 3. Numerical results compared with Mikaelian's theory [5]. Upper row: strong shock ($M_{s,I} = 2$) with negative Atwood number ($A^- = -9/11$); middle row: strong shock ($M_{s,I} = 2$) with positive Atwood number ($A^- = 9/11$); lower row: weak shock ($M_{s,I} = 1.2$) with positive Atwood number ($A^- = 9/11$). Left column: perturbation growth scaled with the natural units. Right column: results scaled using the postshock dimensionless parameters. Good collapsing patterns are observed for strong-shock cases ($M_{s,I} = 2$), among which those with positive Atwood number $A^- = 9/11$ show a good qualitative agreement with Mikaelian's theory [5], whereas the weak-shock cases display poor collapsing under the normalization.

on Mikaelian's model (see Sec. II) are used [Figs. 3(b), 3(d) and 3(f)]. To facilitate comparison of simulation results with Mikaelian's model [5], we also plot in dashed lines the theoretical $\tilde{\eta} - \tilde{t}$ curves for Weber numbers larger than 200, at which the phase shift term $\arctan 1/\sqrt{\mathrm{We}^+}$ becomes negligible.

In the following parts, we will first discuss the influence of Atwood number A^- on postshock perturbation growth in IV A 1 by comparing the first and second row in Fig. 3, and then the influence of incident shock Mach number $M_{s,I}$ in Sec. IV A 2 by comparing the first and third row of the same figure.

1. Effect of initial fluid density configuration

As is shown in Figs. 3(a) and 3(c), when normalized using the natural scheme introduced in Sec. III A, the postshock perturbation amplitude η/λ will first increase with diminishing growth rate. At small postshock Weber number We^+, η/λ will reach a peak and then decrease, whereas for large We^+ values the peak will not be reached in the limited simulation domain. These findings agree with the numerical results of [21].

When the time developments of perturbation are normalized using the scheme developed in Sec. II B [see Figs. 3(d) and 3(f)], they overlap very well for both positive and negative Atwood number cases with $M_{s,i} = 2$. However, discrepancy exists between the two Atwood number classes: the positive Atwood number cases have their first normalized peaks around $\tilde{\eta} = 1.1$ [Fig. 3(b)], while those of the negative Atwood number cases are much higher, being around $\tilde{\eta} = 7.3$ [Fig. 3(d)]. Consequently, the positive Atwood number cases conform to Mikaelian's model Eq. (9) more closely, whereas the negative Atwood number cases show a nontrivial deviation from the same model.

This negative-Atwood discrepancy is rooted in the incompressible nature of Mikaelian's model [5] and might be traced further back to the situations where surface tension σ is absent. As the postshock Weber number We^+ asymptotically approaches infinity, Mikaelian's model [5] will reduce to Richtmyer's impulsive prescription [24] in the form of Eq. (5). Vandenboomgaerde *et al.* [22] and Velikovich [25] observe that this prescription usually gives good results for positive Atwood number cases, but fails for negative Atwood number cases where $\dot{\eta}$ is not proportional to A^+ [23] and other alternatives are available (e.g., Refs. [22,28,36]). In particular, the negative Atwood number is qualitatively different from the positive case, as it generates a reflected rarefaction wave rather than a reflected shock, as noted in Sec. II B. This is the physical reason for this discrepancy.

We will now seek to develop a correction to the linear theory of Ref. [5] that can effectively reduce the discrepancy caused by opposite signs of Atwood numbers. An alternative to Eq. (5) is given in Ref. [22] as

$$\eta = \eta_0^+ + k\Delta v\left[\frac{1}{2}(A^+\eta_0^+ + A^-\eta_0^-) - \frac{1}{6}(A^+ - A^-)(\eta_0^+ - \eta_0^-)\right]t. \tag{17}$$

In this prescription, the postshock perturbation growth rate now depends on both pre- and postshock states, which is different from Mikaelian's model [5], as the latter is only related to the postshock state. According to Ref. [22], this prescription takes into account the shock-induced compression of the perturbation and variation of Atwood number in a simplified way; and while Dimonte [32] notes that this prescription might be problematic when A^+ and A^- are very different, Table I suggests that the two Atwood numbers are very close in our numerical calculations, especially for the negative Atwood number cases where $A^- = -9/11$, in which case Eq. (17) reduces to the following prescription of Meyer and Blewett [28]:

$$\eta = \eta_0^+ + k\Delta v\left[\frac{1}{2}A^+(\eta_0^+ + \eta_0^-)\right]t, \tag{18}$$

which has been reported to match well with the RMI perturbation growth trend in cases with negative A^- [32,37]. Consequently, we expect good performance of Vandenboomgaerde's prescription [22] in the parameter space we explore. We then seek to compare Vandenboomgaerde's prescription [22] with Richtmyer's [24] in the zero-surface-tension cases with different Atwood number setups.

As is shown in Figs. 4(a) and 4(b), we normalize time t and the perturbation amplitude η by the natural units introduced in Sec. III A. It is found that Vandenboomgaerde's prescription Eq. (17)

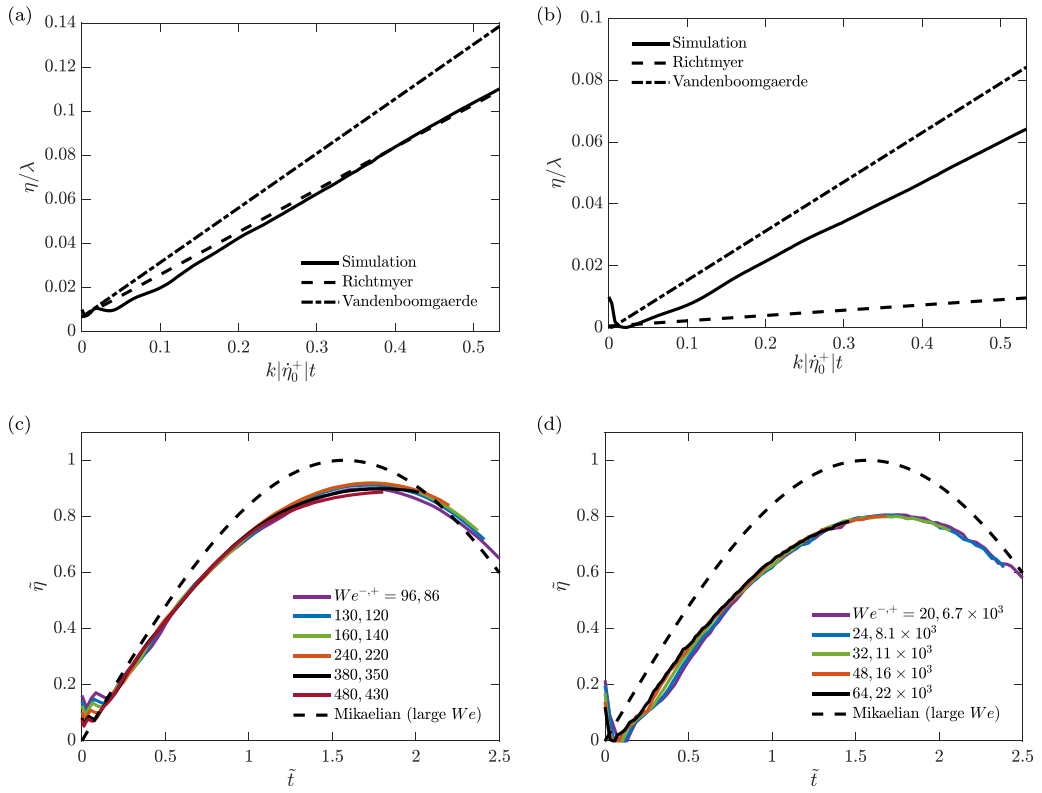

FIG. 4. Upper row: Comparison of the simulation results with the theortical predictions of Richtmyer [24] and Vandenboomgaerde *et al.* [22]. Lower row: simulation results scaled using the modified model in cases with surface tension. (a, c) $A^- = 9/11$, (b, d) $A^- = -9/11$. The theory of Vandenboomgaerde [22] shows a better match with simulation results in both negative and Atwood number cases without surface tension, leading to improved performance of the modified theoretical model.

matches much better with simulation results for the negative Atwood number cases compared with Richtmyer's prescription Eq. (5) [24], and is also close to the numerical results in the positive Atwood number cases. The failure of Richtmyer's prescription [24] for the negative Atwood number case corresponds back to the deviation patterns of our simulation results from the scaling model in the previous part, where the $A^- = 9/11$ cases slightly overshoots the theoretical maximum $\tilde{\eta}_{\max} = 1$ under the scaling, and those with $A^- = -9/11$ significantly overestimates the same maximum.

Consequently, in order to modify Mikaelian's model [5] for a better performance, we tentatively replace the Richtmyer's prescription embodied in Eq. (3) with Vandenboomgaerde's [22]. To this end, we introduce the modified Atwood number $\tilde{A}$ based on Vandenboomgaerde's work [22], which may be viewed as an average of pre- and postshock Atwood numbers A^- and A^+ involving compression ratio $r \equiv \eta_0^+/\eta_0^-$:

$$\tilde{A} \equiv \frac{1}{2}\left(A^+ + \frac{A^-}{r}\right) - \frac{1}{6}(A^+ - A^-)\left(1 - \frac{1}{r}\right). \tag{19}$$

With this modified Atwood number defined, the postshock dimensionless parameters Eqs. (7) and (8) and normalized perturbation-growth model Eq. (9) proposed in Sec. II B can be formally retained by replacing all A^+ with $\tilde{A}$, which is then used to nondimensionalize the results for Figs. 4(c) and 4(d).

When the modified model is compared with simulation results, as is shown in Figs. 4(c) and 4(d), within each Atwood number category the normalized curves still show good collapsing, and good agreement is found between the results of the two Atwood numbers with opposite signs, as the first peaks of all normalized curves are now around $(\tilde{t}, \tilde{\eta}) = (1.65, 0.8)$. This maximum $\tilde{\eta}$ value of 0.8 is less than unity as expected by the modified model, which is likely caused by the aforementioned overestimation of $\dot{\eta}_0^+$ by Vandenboomgaerde's prescription [22] in zero-surface-tension cases; but it is still a considerable improvement compared with the original model of Mikaelian [5], especially for negative Atwood number cases since their discrepancy in peak values with positive Atwood ones is now greatly reduced.

2. Effect of incident shock strength

Apart from surface tension and initial density setups, Mach number of the incident shock $M_{s,i}$ also plays a significant role in the postshock perturbation growth, as it is directly connected with shock strength and effects of compressibility via Eq. (2) [22]. Since Mikaelian's model [5] is essentially impulsive and incorporates Richtmyer's prescription [24], it is natural to expect better matching of the simulation results with our scaled model in the weak shock limit. We find that this is indeed the case for $M_{s,i} = 1.2$, as the perturbation growth patterns shown in Fig. 3(f) are closer to Mikaelian's prediction compared with Fig. 3(b), with maximum normalized perturbation amplitude values almost exactly equaling 1. The recent numerical work by Bigdelou [9] has also confirmed a good match of linear-regime perturbation growth with Mikaelian's prediction for RMI cases with $M_{s,i} = 1.2$, where a different preshock Atwood number $A^- = 2/3$ is used.

We further discuss the applicability of our modification of Mikaelian's model Eq. (9) in Sec. IV A 1. Mikaelian approximates the impact of the incident shock on the interface as an impulsive acceleration, which is compatible with the prescriptions of both Richtmyer [24] and Vandenboomgaerde [22]. More accurate models for perturbation growth under the influence of surface tension can be derived using the same approach in Sec. IV A 1, i.e., swapping Vandenboomgaerde *et al.*'s prescription Eq. (19) for more precise ones, preferably those accounting for nonlinear perturbation development (e.g., Ref. [38]), and combining them with Mikaelian's model, as long as the prescriptions introduced are compatible with the impulsive base of Mikaelian. However, it should be noted that the impulsive model will become inaccurate at higher values of $M_{s,I}$ (see, e.g., the limit of $\epsilon \to 1$ in Fig. 5 of Ref. [11]), where compressible theories predicting perturbation growth have to be proposed. This is a fundamental problem for RMI studies and requires detailed investigation of the shock-interface interaction period, which is out of the scope of this work.

Consequently, we conclude that in the linear oscillation regime with strong surface tension, the scaled model Eq. (9) based on Mikaelian [5] match very well with weak-shock cases, whereas the strong-shock positive Atwood number cases show maximum perturbation values slightly larger than those predicted by Mikaelian due to stronger influence of compressibility. The strong-shock negative Atwood number cases show maximum $\tilde{\eta}$ values that are several times larger than Mikaelian's prediction, but still keep good collapsing patterns under the proposed nondimensionalization scheme Eq. (8). This nontrivial negative-Atwood deviation is due to the well-attested failure of Richtmyer's prescription [5] incorporated in Mikaelian's model, and may be reduced by introducing more accurate prescriptions for postshock initial perturbation growth rate $\dot{\eta}_0^+$.

B. Nonlinear regime

As the simulation cases with incident shock Mach number $M_{s,I} = 1.2$ feature relatively small Weber numbers and weak influence of compressibility, and their perturbation growth patterns are thus close to the prediction of Mikaelian [5], in the following parts we mainly focus on the analysis of the simulation results with $M_{s,I} = 2$.

When surface tension becomes small enough, it can no longer curb the perturbation growth and the development of asymmetric spikes and bubbles on the interface. Figure 5 shows the evolution of a bubble (the broad structure straddling the periodic boundary of the domain) and a spike (the narrow

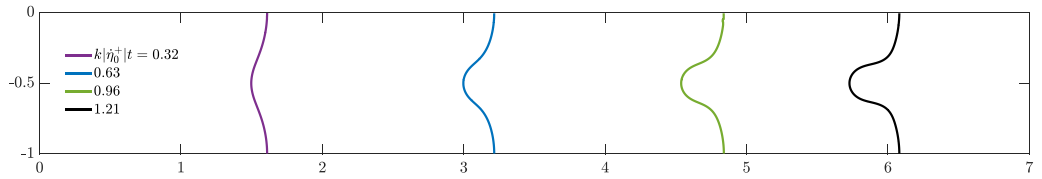

FIG. 5. A series of $We^- = 3800$ simulation snapshots showing the evolution of the perturbed interface from the initially sinusoidal shape to one with a bubble (across the periodic boundaries) and a spike (at the center).

structure near the center of the domain) for $We^- = 3800$. As the surface tension is very small, the asymmetry between bubbles and spikes becomes evident as the nondimensional time $k|\dot{\eta}_0^+|t$ approaches unity, as reported by Dimonte [31] for the onset of nonlinear effects in RMI without surface tension. Sizes of the bubble and the spike can be calculated by measuring the difference between the local and average interface positions, whose time derivatives yield bubble velocity U_B and spike velocity U_S.

The development of calculated bubble velocities U_B and spike velocities U_S at different Weber numbers are first nondimensionalized using the natural units discussed in Sec. III A, and then shown in Fig. 6. The development patterns of bubble velocity are almost the same initially for different Weber numbers, displaying early-time damped oscillating behavior followed by a constantly decreasing period, which agree well in trend with Ref. [39], where front-tracking simulations are used. Similar early-time oscillations of bubble and spike velocities have been observed in Ref. [34], where compressibility is involved, but are lacking in works focusing on incompressible flows (e.g., Refs. [13,40]), indicating that this is an effect of compressibility. Mikaelian [23] reported the oscillations of perturbation growth rate $\dot{\eta}$, and ascribed it to the "rippling" behavior of the transmitted and reflected shocks; i.e., the profile of the two shocks are gradually flattened after they travel a distance of magnitude $\lambda = D$ away from the interface, as is also noted in Sec. II.

Within the decreasing phase of bubble growth rate, for the cases with preshock Weber numbers less than ∼500, the "bubble velocity" (more precisely, the growth rate of the sinusoidal crests as bubbles have not yet formed in these cases) eventually decreases below 0 due to the long-term restoring effect of surface tension. As the Weber number is further increased, the curves remain positive for the entire simulated time and become less sensitive to preshock Weber number beyond

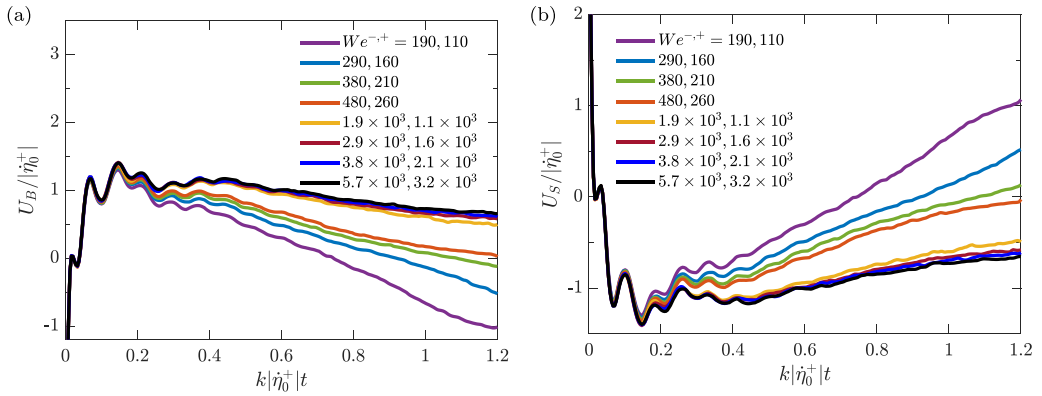

FIG. 6. Development of bubble (a) and spike (b) velocity for transitional and nonlinear cases with $A^- = 9/11$. As Weber number increases, the curbing effect of surface tension on the postshock perturbation growth diminishes, and the time development patterns of bubble and spike velocities remain roughly the same within a large range of high Weber numbers (greater than 10^3).

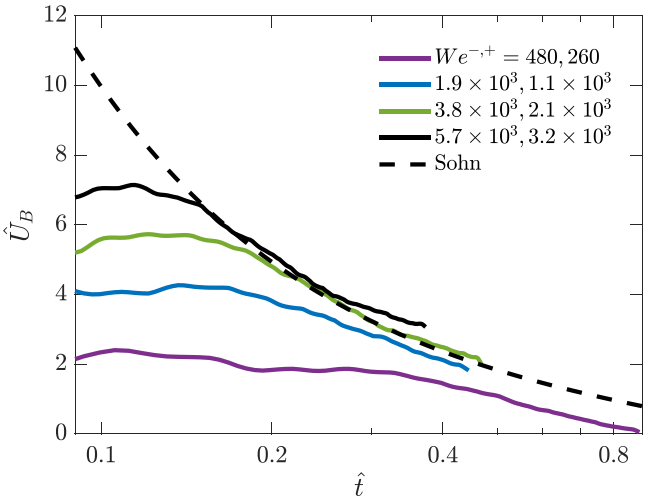

FIG. 7. Comparison between simulated (solid lines) and theoretical (dashed line) bubble velocity developments in cases with $\mathrm{We}^- = 480$, 1900, 3800, and 5700. Good agreements with Sohn's theory are found at asymptotically large Weber numbers.

$\sim$1900 (i.e., postshock Weber number We^+ beyond 1100, which we consider as the lower bound of the nonlinear regime, as noted in Sec. I). This indicates that within this range of Weber numbers, the development of bubbles velocity departs from an oscillatory regime and approaches asymptotically zero velocity. The absolute values of spike velocities $|U_S|$ in the high Weber number cases are also decreasing after the oscillation period, similar to that of the bubble velocity.

Based on potential flow methods, Sohn derived a nonlinear and incompressible model in Ref. [13] for the late-time bubble development, which accounts for effects of both viscosity and surface tension in RMI at the same time. A similar model is also proposed in Ref. [41]. Specifically, when the two fluids are inviscid, the nondimensional expression of Sohn's model [13] reads

$$\hat{U}_B = \cot \hat{t}, \tag{20}$$

where

$$\hat{U}_B \equiv \frac{3}{A^+}\sqrt{\frac{(1+A^+)\mathrm{We}^+}{2}}\frac{U_B}{\Delta v}, \quad \hat{t} \equiv \frac{\sqrt{2(1+A^+)}}{3+A^+}\tilde{t} = \frac{\sqrt{2(1+A^+)}}{3+A^+}\frac{kA^+\Delta v}{\sqrt{\mathrm{We}^+}}t. \tag{21}$$

Note that the nondimensional Eq. (21) is not derived from the model of Mikaelian [Eqs. (8) and (9)], which is not applicable in the regime with asymptotically small surface tension discussed here. Rather, the postshock nondimensional parameters defined in Eq. (7) are retained to reformulate Sohn's nonlinear theory for consistency.

We now seek to compare our measured bubble velocities with Sohn's model [13]. For this purpose, we normalize bubble velocity and time extracted from simulation cases with $\mathrm{We}^- = 480$, 1900, 3800, and 5700 according to the definitions of $\hat{U}_B$ and $\hat{t}$. The normalized curves are plotted in Fig. 7 and compared with Sohn's model [13] in the form of Eq. (20).

As is shown in Fig. 7, for the transitional Weber number case with $\mathrm{We}^- = 480$, Sohn's model [13] significantly overestimates the U_B development within the simulated time range, despite correctly capturing the late-time decreasing trend. As for the cases with higher Weber numbers exceeding 10^3, where surface tension is weak enough to give way to formation of bubbles and spikes, the normalized simulation results asymptotically converges to Sohn's cotangent model [13] as normalized time $\hat{t}$ increases. Also, as the Weber number increases, convergence to Sohn's model [13] will occur at earlier normalized time $\hat{t}$. This verifies that Sohn's model [13] applies for

asymptotically high Weber numbers, since, for lower Weber numbers, surface tension still has some curbing effects on the development of bubbles and spikes.

Within Sohn's text [13], Eq. (20) is defined for asymptotically large We^+ so that the singularity at $\hat{t} = \pi/2$ is not reached for any physical time t. However, our simulations feature large but finite We^+, so that for sufficiently large physical time t, the $\hat{t} = \pi/2$ singularity may be reached in simulations. This may correspond with the bubble velocity becoming negative and the interface thus exhibiting nascent oscillatory behavior, as speculated by Sohn [13].

Therefore, we conclude that within the time range investigated, our results agree well with Sohn's model [13] in the bubble-development period of very high Weber number cases, besides the inability of Sohn's model to capture the early oscillatory behavior of the bubble and spike velocities, due to compressible effects, observed in this study. The development of spikes and bubbles at later time remains to be investigated, where Dimonte [32] reports that bubble amplitudes will eventually saturate due to nonlinear effects; and in the meantime spikes will continually grow and eventually break off from the interface, as has been predicted by Sohn [13] and Matsuoka [15,42], and recently observed in simulations by Corot *et al.* [21].

C. Transition to the nonlinear regime

In Sec. IV A, we discussed the linear regime of interface evolution, which occurs for small Weber numbers (strong surface tension), for which the interface perturbations oscillate with small amplitude. Then, in Sec. IV B, we discussed the late-time development of the highly nonlinear bubbles and spikes, which appear for large Weber numbers (small surface tension). However, for intermediate Weber numbers the surface tension may curb but not prevent transition into a nonlinear evolution regime, which still exhibits oscillatory behavior. The preshock initial perturbation slope s^- also plays a significant role in the later transition process, as larger s^- values result in more rapid depositions of baroclinic vorticity at the interface, which causes it to evolve from the initially sinusoidal shape into the complex late-time structures [40]. Therefore, both slope and Weber number will determine the nonlinear transition. Since the nondimensional formulation Eqs. (7) and (8) is based on the linear incompressible theory of Mikaelian [5], it is used in this section to diagnose the departure from the linear regime, and to develop a heuristic criterion for transition to nonlinear behavior.

First, we seek a quantitative indicator of nonlinear transition. The earliest such signature is the departure from the sinusoidal oscillation predicted by the linear theory. Therefore, as Weber number and slope increase, nonlinear deviations in the shape of the $\tilde{\eta} - \tilde{t}$ curves are expected to be found first near the normalized peaks, as the onset of nonlinearity should be relatively subtle and achieved most easily at maximum amplitudes. Figures 8(a), 8(b) and 8(c) show the first peak of the perturbation oscillation as a function of Weber number, each at a different slope s^-. In these figures, the axes are normalized according to the linear theory [5].

For each s^-, corresponding with each of Figs. 8(a), 8(b) and 8(c), the peaks of the perturbation amplitude curves are marked out. In each case, the peak perturbation amplitude first increases, then decreases with increasing We^-. The time of peak amplitude, however, increases with We^- in all cases. We also note that this phenomenon becomes apparent at lower Weber numbers for the cases $s^- = 0.03\pi, 0.04\pi$ [Figs. 8(b) and 8(c)] than at $s^- = 0.02\pi$ [Fig. 8(a)]. The phase shift that occurs with increasing We^- cannot be explained by the change of $\Delta\varphi = \arctan 1/\sqrt{We^+}$ alone in Eq. (9); for example, the phase-shift value predicted by this term for the $s^- = 0.02\pi$ cases with We^+ between 130 and 260 is only 0.025, much less than the measured value of 0.05 in Fig. 8(a). Since the phase shift we observed in Figs. 8(a), 8(b) and 8(c) occurs around postshock Weber number $We^+ \sim 10^2$, we select 10^2 as the typical Weber number for the lower bound of the transitional regime and the upper bound of the linear oscillatory regime, as also noted in Sec. I; while a more rigorous criterion incorporating the influence of the slope s^- will be proposed below.

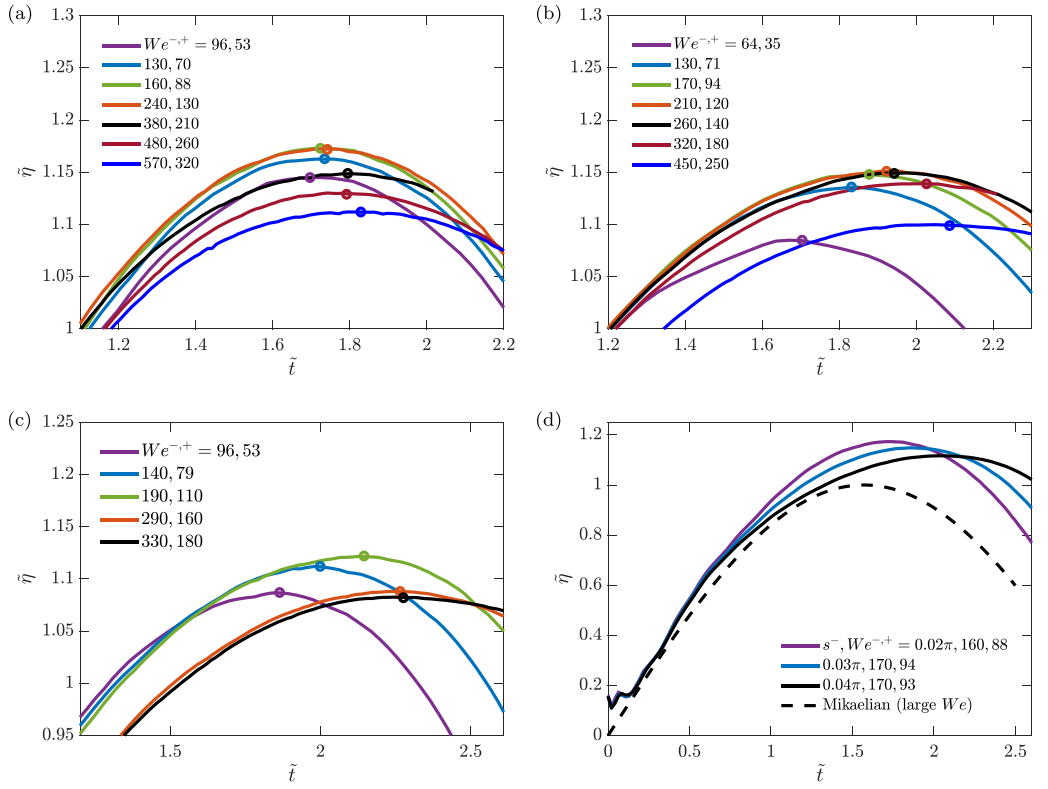

FIG. 8. Normalized perturbation development curves for $A^- = 9/11$. (a) $s^- = 0.02\pi$; (b) $s^- = 0.03\pi$; (c) $s^- = 0.04\pi$; (d) comparisons of cases with $s^- = 0.02\pi$, 0.03π, and 0.04π, at We^+ values around 90. For panels (a–c), the zoom-in views near the first peaks of the curves are displayed, and the peak points of each curve are marked with circles. Rightward shift of the peak points is found as the nonlinear indicator.

We also varied s^- at constant $\mathrm{We}^+ \simeq 90$ to study the effect of amplitude alone [Fig. 8(d)]. Compared with the nonlinear effects of increasing Weber number, the rightward phase shift caused by increasing s^- occurs at a global scale, as the normalized curves start to diverge at $\tilde{t} \approx 0.65$, while the peak values decrease slightly as s^- increases. Again, this rightward shift cannot be explained by the change of $\Delta\varphi = \arctan 1/\sqrt{\mathrm{We}^+}$ in Eq. (9), as the term does not explicitly contain s^-, and are almost the same for the three cases as the postshock Weber numbers We^+ are nearly fixed. The initial amplitude of perturbation therefore has a material effect on the critical Weber number required for nonlinear transition.

Therefore, nonlinear transition appears to manifest most clearly as a shift in (normalized) time of the peak of the first oscillation. We quantify this directly as the relative error between the detected peak time (normalized, denoted $\tilde{t}_m$), and that predicted by the linear theory,

$$\Delta \equiv \left| \frac{\tilde{t}_m}{\frac{\pi}{2} - \arctan \frac{1}{\sqrt{\mathrm{We}^+}}} - 1 \right|. \tag{22}$$

Note that this is defined according to the postshock Weber number, We^+. For properly linear evolution, $\Delta = 0$, corresponding to exact matching with the linear theory of Ref. [5], but this is not attained for any cases in this study for even the smallest We^-, s^- with incident shock number $M_{s,I} = 2$, primarily due to strong effects of compressibility as discussed in Sec. IV A. Of course, the transition to nonlinearity is also gradual, so that a critical value Δ_c for nonlinear transition can only

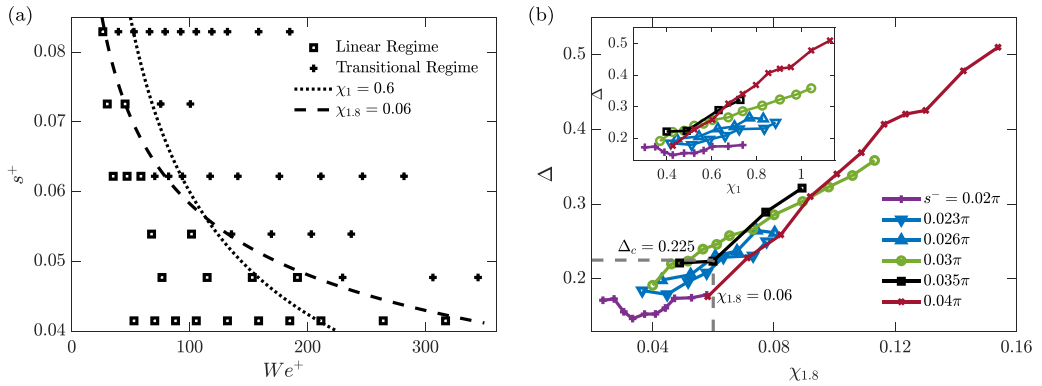

FIG. 9. Left: phase diagram showing simulation cases in linear growth-rate regime (squares) and transitional regime (crosses). The boundary between the two is selected as $\chi_{1.8} = 0.06$ and plotted in dashed line, while $\chi_1 = 0.6$ is also plotted in dotted line for comparison. Right: relationship between Δ and $\chi_{1.8}$ with different s^- setups. A common growth stage of Δ is reached for different s^- setups as $\chi_{1.8}$ increases, and the critical Δ_c and $\chi_{1.8}$ values are plotted.

be heuristically chosen. Here we first choose $\Delta_c = 0.255$, and plot in Fig. 9(a) a phase diagram that identifies linear cases ($\Delta < \Delta_c$, in yellow squares) and transitional cases ($\Delta \geqslant \Delta_c$, in blue pluses).

We now seek a simple predictive model for Δ and Δ_c, in order to identify the presence of nonlinear effects due to the effect of Weber number We^+ and postshock perturbation slope s^+. The criterion $k|\dot{\eta}_0^+|t \sim 1$ proposed by Dimonte [31] is not applicable in this section as surface tension may significantly influence the transition mechanism. We therefore assume heuristically that nonlinear effects become apparent when the peak perturbation amplitude-to-wavelength ratio reaches ∼0.1, or equivalently when $s_{\max} \equiv k\eta_{\max} \sim 0.6$ (Bigdelou [9] proposed a similar criterion of $k\eta_{\max} \sim 1$). From Eqs. (7) and (8) and for $\mathrm{We}^+ \gg 1$, this suggests that transition begins to occur for values of the parameter $\chi_1 \simeq 0.6$, where

$$\chi_\alpha \equiv (s^+)^\alpha \sqrt{\mathrm{We}^+} \tag{23}$$

and $\alpha = 1$ as a first estimate.

We plot $\chi_1 = 0.6$ in Fig. 9(a) as a dotted line, but it does not correctly delineate linear and transitional cases for the given choice of Δ_c. Moreover, as shown in the inset of Fig. 9(b), χ_1 does not fully explain the variation in Δ. In that plot, while Δ increases with χ_1, the rate of increase is clearly dependent on s^- (hence, s^+). There is therefore a further dependence of the transition to nonlinearity on s^+, suggesting a better choice of α in Eq. (23), which may be related to the local competition of surface tension and baroclinic vorticity on the interface, and awaits a more detailed investigation. Figure 9(b) shows the resulting scaling with a modified $\chi_{1.8}$ where $\alpha = 1.8$, which better collapses the data. Plotting the dashed line $\chi_{1.8} = 0.06$ on Fig. 9(a) also more clearly delineates the linear and nonlinear cases, especially for those with larger perturbation slope s^+. The measure is not perfect, as it does not fully delineate all linear and transitional cases. We attribute this to the curves not fully collapsing in Fig. 9(b). Nevertheless, for any choice of Δ_c a critical value for $\chi_{1.8}$ can always be found that reasonably separates those conditions that will remain linear from those that transit to nonlinear behavior.

V. CONCLUSIONS

We have presented results of nonlinear and compressible numerical simulations of the Richtmyer-Meshkov instability with surface tension in the linear, nonlinear and transitional regime

of perturbation development. Our core results are summarized below corresponding to each perturbation development regime, with the Weber number range of each regime highlighted:

First, in the *linear regime* where $\mathrm{We}^+ < 10^2$, using appropriate dimensional analysis, we find that the existing theoretical impulsive model due to Mikaelian [5] predicts well the evolution of the shocked interface in this regime, with an appropriate modification based on the theory of Vandenboomgaerde [22] to accommodate Atwood numbers of either sign.

Next, in the *nonlinear regime* where $\mathrm{We}^+ > 10^3$, we show agreement with theoretical predictions of Sohn [13] on the asymptotic (large time) bubble velocity in the limit of large Weber number, while a complete quantitative comparison of bubble and spike behavior at late times is left for future work.

Finally, in the *transitional regime* where $10^2 \leqslant \mathrm{We}^+ \leqslant 10^3$, we use Eq. (8) to diagnose the onset of this regime to allow for comparison with results in the linear oscillatory regime, and develop a heuristic criterion based on nondimensional parameters s^+ and We^+ for transition to nonlinear development.

These results indicate the utility of this numerical model for problems involving multiphase compressible flows, and constitute a further validation of its surface tension model and implementation. This study sheds light on influence of surface tension on the compressible RMI, which is important for related multiphase compressible flow problems where surface tension effects have not yet been systematically investigated, for example, shock-bubble interactions [19]; while also providing a stepping stone towards the mixed compressible-incompressible problem which may influence the early-time development of the shocked-droplet or aerobreakup problem [43].

ACKNOWLEDGMENTS

This work has been supported by the National Science Foundation under CAREER Award No. 1844932 (Bubble Fragmentation in Turbulent Flows) to L.D. We acknowledge the anonymous reviewers for their constructive comments which helped improve the manuscript, and K.T. thanks the Tsinghua-Princeton Undergraduate Exchange Program for enabling this research to take place.

APPENDIX A: NUMERICAL CONVERGENCE AND MAXIMUM RESOLVABLE WEBER NUMBER

Since each fluid is inviscid, the smallest length scale in the bulk is set by numerical dissipation, so that pointwise grid convergence is not expected. Nevertheless, we require that the primary characteristics of the RMI growth, both with and without surface tension, be independent of grid resolution at our chosen resolution of $L = 9$. Here, four groups of convergence tests are conducted in total for four different categories of initial setups; namely, light-heavy ($A^- > 0$) and heavy-light ($A^- < 0$) density setups with and without surface tension. Specifically, we set $A^- = \pm 9/11$, while $\mathrm{We}^- = +\infty$ or 160.

The raw outputs of the tests are provided in Fig. 10, where time t and perturbation η are normalized by the natural units introduced in Sec. III A. Absolute values are taken to facilitate the comparison between the results of light-heavy and heavy-light initial density setups, as in the latter case there will be a phase reversal of the perturbation profile at early time. When relatively weak surface tension is introduced to the heavy-light density setup case or the resolution level L is low, noise may appear in the neighborhood of the interface during the simulation, causing spurious high-frequency oscillations on the curve. Despite these problems, we still observe good converging trend at resolution level $L = 9$ for all four groups of convergence tests.

As Sec. IV B investigates RMI with asymptotically weak surface tension, it is also of interest to determine the maximum Weber number We_m resolvable at a certain resolution level. This is achieved by setting the following grid Weber number $\mathrm{We}_{\mathrm{grid}}$ to 1:

$$\mathrm{We}_{\mathrm{grid}} \equiv \frac{(\rho_1^+ + \rho_2^+)(\dot{\eta}_0^+)^2 h}{\sigma_c}, \tag{A1}$$

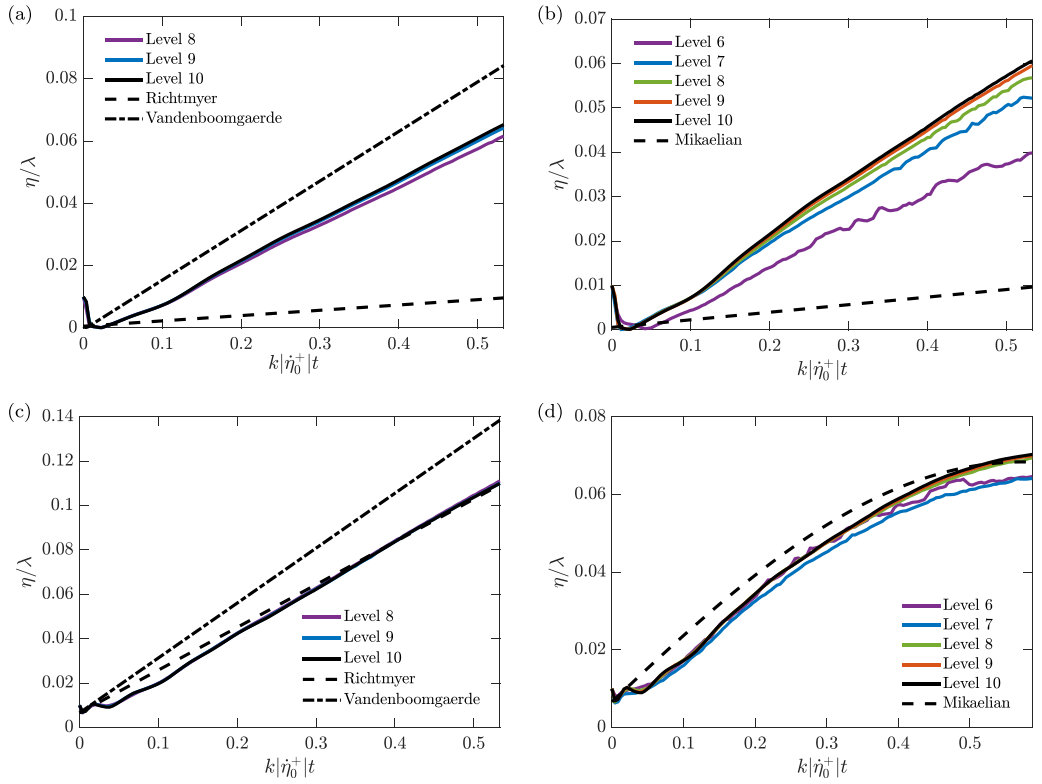

FIG. 10. Convergence test results (Upper row: heavy-light density setup without (a) and with (b) surface tension; lower row: light-heavy density setup without (c) and with (d) surface tension). Good numerical convergence is observed for all the inviscid test cases.

and the critical surface tension σ_c is then plugged into the definition of postshock Weber number We^+ as given by Eq. (7). We then find that for the positive Atwood number cases at resolution level $L = 9$, the maximum resolvable Weber number is

$$\mathrm{We}_m = \frac{1}{k^3(\eta_0^+)^2 h} = 4.7 \times 10^4, \tag{A2}$$

which is much larger than the maximum postshock Weber number investigated in this work (3.2×10^3), and we therefore expect that our numerical results effectively capture surface tension at the Weber numbers and resolutions that were tested.

APPENDIX B: DETERMINATION OF POSTSHOCK STATE

While in this study, the postshock state is determined through numerical diagnostics, it is instructive to compare them with theoretical predictions.

If surface tension and interface perturbation are absent, then the flow state constitutes a Riemann problem when the incident shock arrives at the interface, whose solution yields the postshock state. Mikaelian [23] proposes a set of equations for this problem. Lying at the core of this equation system are two alternative transcendental equations (Eqs. (A4) and (A16) in the Appendix of Ref. [23]) for

which there are generally no analytical solutions:

$$\frac{\xi-\frac{p_0}{p_L}}{\sqrt{\xi+\frac{\gamma-1}{\gamma+1}\frac{p_0}{p_L}}}=\begin{cases}\sqrt{\frac{\rho_2^-}{\rho_1^-}}\cdot\dfrac{1-\frac{p_0}{p_L}-(\xi-1)\sqrt{\frac{\gamma-1+(\gamma+1)\frac{p_0}{p_L}}{(\gamma+1)\xi+\gamma-1}}}{\sqrt{1+\frac{\gamma-1}{\gamma+1}\frac{p_0}{p_L}}}, & \xi\geqslant 1,\\ \sqrt{\frac{\rho_2^-}{\rho_1^-}}\cdot\dfrac{1-\frac{p_0}{p_L}+\left(1-\xi^{\frac{\gamma-1}{2\gamma}}\right)\sqrt{\frac{2\gamma}{\gamma-1}+\frac{\gamma+1}{(\gamma-1)^2}\frac{p_0}{p_L}}}{\sqrt{1+\frac{\gamma-1}{\gamma+1}\frac{p_0}{p_L}}}, & \xi<1.\end{cases}\tag{B1}$$

The first equation is physically valid when its root satisfies $\xi\geqslant 1$, which indicates a reflected shock; otherwise, the second one will produce a root satisfying $\xi\leqslant 1$, which indicates a reflected rarefaction instead. Once the value of ξ has been determined, the postshock quantities ρ_i^+, Δv can be determined via the following equations:

$$\begin{aligned}\frac{\rho_1^+}{\rho_1^-}&=\begin{cases}\dfrac{(\gamma+1)+(\gamma-1)\frac{p_0}{p_L}}{(\gamma-1)+(\gamma+1)\frac{p_0}{p_L}}\cdot\dfrac{(\gamma+1)\xi+\gamma-1}{(\gamma-1)\xi+\gamma+1}, & \xi\geqslant 1\\ \dfrac{(\gamma+1)+(\gamma-1)\frac{p_0}{p_L}}{(\gamma-1)+(\gamma+1)\frac{p_0}{p_L}}\cdot\xi^{\frac{1}{\gamma}}, & \xi<1\end{cases},\\ \frac{\rho_2^+}{\rho_2^-}&=\frac{(\gamma+1)\xi+(\gamma-1)\frac{p_0}{p_L}}{(\gamma-1)\xi+(\gamma+1)\frac{p_0}{p_L}},\\ (\Delta v)^2&=\frac{2\xi p_L}{\rho_2^-}\cdot\frac{\left(1-\frac{p_0}{\xi p_L}\right)^2}{(\gamma+1)+(\gamma-1)\frac{p_0}{\xi p_L}}.\end{aligned}\tag{B2}$$

It should be noted that Eqs. (B1) and (B2) do not include effects of surface tension or the perturbed interface profile investigated in our work. Both factors could potentially cause the postshock state to deviate from the solution of the Riemann problem. In particular, the perturbed interface profile gives rise to the RMI, and causes the transmitted and reflected wavefronts to have corrugated shapes initially, which are similar to the sinusoidal shape of the perturbed interface itself. These wavefront corrugations will oscillate and die out after the waves travel a distance of several wavelengths away from the postshock interface [44], as is the situation shown in Fig. 1(b). This rippling behavior has been observed in the experiments of Ref. [45], and reproduced afterwards in many simulation works (e.g., Refs. [23,39,46]).

We compare now the predictions of theory and numerical diagnostics for the cases presented in Fig. 2. The transcendental equation sets [Eqs. (B1) and (B2)] yields $\xi=1.8982$ for the cases with $A^-=9/11$, and $\xi=0.4668$ for those with $A^-=-9/11$. These solutions agree with the categorization of reflected wave [Eq. (10)] by Drake [27], which is based on the sign of preshock Atwood number A^-.

The postshock parameters are then derived using the solution ξ, and their comparisons with the values of numerical diagnostics measured at around $t=0.4$ are shown in the following Table I. Here $r\equiv\eta_0^+/\eta_0^-$ is the compression ratio of perturbation amplitude, which may be calculated by $r=1-\Delta v/u_{s,I}$ according to Refs. [22,23].

Within each preshock Atwood number category, the results gained via numerical diagnostics and equation solving for the same postshock parameter are roughly on the same level of magnitude. Particularly good agreements are found for ρ_2^+ values in cases with $A^-=-9/11$, and also A^+ and r in those with $A^-=9/11$. However, generally speaking, nontrivial discrepancies do exist between the numerical and analytical results.

The discrepancies are most likely caused by the equation system Eq. (B1)'s not accounting for the influence of the "rippling" behavior of the postshock wavefronts due to the initially perturbed

TABLE I. Comparison between postshock values gained from numerical diagnostics ("ND") and equation solving ("ES").

A^- (Method)	9/11 (ND)	9/11 (ES)	−9/11 (ND)	−9/11 (ES)
ρ_1^+	0.356	0.418	1.700	1.591
ρ_2^+	3.084	3.593	0.169	0.168
A^+	0.793	0.792	−0.819	−0.809
Δv	2.030	2.333	2.231	2.109
r	0.66	0.688	0.0565	0.109

interface profile (see Sec. II). In cases without surface tension, such behavior is reported in Ref. [23] to cause the postshock perturbation growth rate $\dot{\eta}$ to reach an asymptotic value, for which no simple analytic solution exists [23,47], after going through a damped oscillation period, which also matches the trend of our results in Fig. 2.

The ascription of discrepancies above is further consolidated by the following observation. As is shown in Fig. 2, for the case with $A^- = 9/11$, our state diagnostic case captures $\rho_1^+ = 0.411$ and $\rho_2^+ = 3.590$ at a very early time $t = 0.02$ after the shock-interface interaction, which matches very well with the solution of Mikaelian's equation sets [23] (see column 3 of Table I). However, the two densities eventually settle down at the steady-state values, as discussed in Sec. IV A.

The relationship between pre- and postshock Weber numbers We^- and We^+ may now be derived using the postshock states determined by numerical diagnostics, which enables direct prediction of We^+ from We^-. Based on the definitions of We^- and We^+ [Eqs. (1) and (7)], we find that

$$\frac{\mathrm{We}^+}{\mathrm{We}^-} = \frac{\rho_1^+ + \rho_2^+}{\rho_1^- + \rho_2^-}\left(\frac{A^+\Delta v}{A^- u_L}\right)^2. \tag{B3}$$

That is, the postshock Weber number depends only on the ratio of postshock to preshock densities, and the Mach number of the incident shock, and is independent of the (small) preshock perturbation amplitude η_0^-. As a result, for simulation cases with preshock Atwood numbers $A^- = 9/11$ and $-9/11$, we have $\mathrm{We}^+/\mathrm{We}^- = 0.553$ and 3.875, respectively.

[1] J. Lindl, O. Landen, J. Edwards, Ed Moses, and NIC team, Review of the national ignition campaign 2009–2012, Phys. Plasmas **21**, 020501 (2014).

[2] N. Gibbons, R. Gehre, S. Brieschenk, and V. Wheatley, Blast wave-induced mixing in a laser ignited hypersonic flow, J. Fluids Eng. **140**, 050902 (2018).

[3] D. Arnett, The role of mixing in astrophysics, Astrophys. J., Suppl. Ser. **127**, 213 (2000).

[4] T. Sano, K. Nishihara, C. Matsuoka, and T. Inoue, Magnetic field amplification associated with the Richtmyer-Meshkov instability, Astrophys. J. **758**, 126 (2012).

[5] K. O. Mikaelian, Rayleigh-Taylor and Richtmyer-Meshkov instabilities in multilayer fluids with surface tension, Phys. Rev. A **42**, 7211 (1990).

[6] P. Carlès and S. Popinet, The effect of viscosity, surface tension and nonlinearity on Richtmyer–Meshkov instability, Eur. J. Mech.-B/Fluids **21**, 511 (2002).

[7] T. G. Theofanous, Aerobreakup of Newtonian and viscoelastic liquids, Annu. Rev. Fluid Mech. **43**, 661 (2011).

[8] J. C. Meng and T. Colonius, Numerical simulation of the aerobreakup of a water droplet, J. Fluid Mech. **835**, 1108 (2018).

[9] P. Bigdelou, A numerical study of interfacial instabilities in shocked materials with surface tension, PhD. thesis, The University of North Carolina at Charlotte, 2020.

[10] S. Osher and R. Fedkiw, *Level-Set Methods and Dynamic Implicit Surfaces*, Vol. 153 (Springer Science & Business Media, Berlin, 2006).
[11] M. Brouillette, The Richtmyer-Meshkov instability, Annu. Rev. Fluid Mech. **34**, 445 (2002).
[12] S. I. Abarzhi and M. Herrmann, New type of the interface evolution in the Richtmyer-Meshkov instability, Technical report, Center for Turbulence Research, Stanford, CA (2003).
[13] S.-Ik Sohn, Effects of surface tension and viscosity on the growth rates of Rayleigh-Taylor and Richtmyer-Meshkov instabilities, Phys. Rev. E **80**, 055302(R) (2009).
[14] H. Ding, P. D. M. Spelt, and C. Shu, Diffuse interface model for incompressible two-phase flows with large density ratios, J. Comput. Phys. **226**, 2078 (2007).
[15] C. Matsuoka, Vortex sheet motion in incompressible Richtmyer–Meshkov and Rayleigh–Taylor instabilities with surface tension, Phys. Fluids **21**, 092107 (2009).
[16] J. Garnier, C. Cherfils-Clerouin, and P.-A. Holstein, Statistical analysis of multimode weakly nonlinear Rayleigh-Taylor instability in the presence of surface tension, Phys. Rev. E **68**, 036401 (2003).
[17] H.-Y. Guo, L.-F. Wang, W.-H. Ye, J.-F. Wu, and W.-Y. Zhang, Weakly nonlinear Rayleigh–Taylor instability in incompressible fluids with surface tension, Chin. Phys. Lett. **34**, 045201 (2017).
[18] Y. Zhou, Rayleigh–Taylor and Richtmyer–Meshkov instability induced flow, turbulence, and mixing. I, Phys. Rep. **720–722**, 1 (2017).
[19] D. Ranjan, J. Oakley, and R. Bonazza, Shock-bubble interactions, Annu. Rev. Fluid Mech. **43**, 117 (2011).
[20] D. Fuster and S. Popinet, An all-mach method for the simulation of bubble dynamics problems in the presence of surface tension, J. Comput. Phys. **374**, 752 (2018).
[21] T. Corot, P. Hoch, and E. Labourasse, Surface tension for compressible fluids in ale framework, J. Comput. Phys. **407**, 109247 (2020).
[22] M. Vandenboomgaerde, C. Mügler, and S. Gauthier, Impulsive model for the Richtmyer-Meshkov instability, Phys. Rev. E **58**, 1874 (1998).
[23] K. O. Mikaelian, Freeze-out and the effect of compressibility in the Richtmyer-Meshkov instability, Phys. Fluids **6**, 356 (1994).
[24] R. D. Richtmyer, Taylor instability in shock acceleration of compressible fluids, Commun. Pure Appl. Math. **13**, 297 (1960).
[25] A. L. Velikovich, Analytic theory of Richtmyer–Meshkov instability for the case of reflected rarefaction wave, Phys. Fluids **8**, 1666 (1996).
[26] A. L. Velikovich, M. Herrmann, and S. I. Abarzhi, Perturbation theory and numerical modelling of weakly and moderately nonlinear dynamics of the incompressible Richtmyer-Meshkov instability, J. Fluid Mech. **751**, 432 (2014).
[27] R. P. Drake, *Shocks and Rarefactions* (Springer, Berlin, 2006), pp. 107–167.
[28] K. A. Meyer and P. J. Blewett, Numerical investigation of the stability of a shock-accelerated interface between two fluids, Phys. Fluids **15**, 753 (1972).
[29] S. Popinet, An accurate adaptive solver for surface-tension-driven interfacial flows, J. Comput. Phys. **228**, 5838 (2009).
[30] S. Popinet, Numerical models of surface tension, Annu. Rev. Fluid Mech. **50**, 49 (2018).
[31] G. Dimonte and P. Ramaprabhu, Simulations and model of the nonlinear Richtmyer–Meshkov instability, Phys. Fluids **22**, 014104 (2010).
[32] G. Dimonte, A modal wave-packet model for the multi-mode Richtmyer–Meshkov instability, Phys. Fluids **33**, 014108 (2021).
[33] J. U. Brackbill, D. B. Kothe, and C. Zemach, A continuum method for modeling surface tension, J. Comput. Phys. **100**, 335 (1992).
[34] R. L. Holmes, G. Dimonte, B. Fryxell, M. L. Gittings, J. W. Grove, M. Schneider, D. H. Sharp, A. L. Velikovich, R. P. Weaver, and Q. Zhang, Richtmyer–Meshkov instability growth: Experiment, simulation and theory, J. Fluid Mech. **389**, 55 (1999).
[35] A. D. Kotelnikov, J. Ray, and N. J. Zabusky, Vortex morphologies on reaccelerated interfaces: Visualization, quantification, and modeling of one-and two-mode compressible and incompressible environments, Phys. Fluids **12**, 3245 (2000).

[36] J. G. Wouchuk and K. Nishihara, Asymptotic growth in the linear Richtmyer–Meshkov instability, Phys. Plasmas **4**, 1028 (1997).
[37] Y. Yang, Q. Zhang, and D. H. Sharp, Small amplitude theory of Richtmyer–Meshkov instability, Phys. Fluids **6**, 1856 (1994).
[38] Q. Zhang and S.-Ik Sohn, An analytical nonlinear theory of Richtmyer-Meshkov instability, Phys. Lett. A **212**, 149 (1996).
[39] R. L. Holmes, J. W. Grove, and D. H. Sharp, Numerical investigation of Richtmyer–Meshkov instability using front tracking, J. Fluid Mech. **301**, 51 (1995).
[40] C. Matsuoka, K. Nishihara, and Y. Fukuda, Nonlinear evolution of an interface in the Richtmyer-Meshkov instability, Phys. Rev. E **67**, 036301 (2003).
[41] M. R. Gupta, R. Banerjee, L. K. Mandal, R. Bhar, H. C. Pant, M. Khan, and M. K. Srivastava, Effect of viscosity and surface tension on the growth of Rayleigh–Taylor instability and Richtmyer–Meshkov instability induced two fluid interfacial nonlinear structure, Indian Journal of Physics **86**, 471 (2012).
[42] C. Matsuoka, Nonlinear behavior of a vortex sheet in incompressible Richtmyer–Meshkov instability with surface tension, Phys. Scr. **2008**, 014042 (2008).
[43] T. G. Theofanous, V. V. Mitkin, C. L. Ng, C. H. Chang, X. Deng, and S. Sushchikh, The physics of aerobreakup. II. Viscous liquids, Phys. Fluids **24**, 022104 (2012).
[44] K. Nishihara, J. G. Wouchuk, C. Matsuoka, R. Ishizaki, and V. V. Zhakhovsky, Richtmyer–Meshkov instability: Theory of linear and nonlinear evolution, Phil. Trans. R. Soc. A **368**, 1769 (2010).
[45] E. E. Meshkov, Instability of the interface of two gases accelerated by a shock wave, Fluid Dyn. **4**, 101 (1969).
[46] K. O. Mikaelian, Effect of viscosity on Rayleigh-Taylor and Richtmyer-Meshkov instabilities, Phys. Rev. E **47**, 375 (1993).
[47] G. Fraley, Rayleigh–Taylor stability for a normal shock wave–density discontinuity interaction, Phys. Fluids **29**, 376 (1986).